



Passive simulation of the nonlinear port-Hamiltonian modeling of a Rhodes Piano

Antoine Falaize^{*,1}, Thomas Hélie¹

Project-Team S3 (Sound Signals and Systems) and Analysis/Synthesis team, Laboratory of Sciences and Technologies of Music and Sound (UMR 9912), IRCAM-CNRS-UPMC, 1 place Igor Stravinsky, F-75004 Paris, France

ARTICLE INFO

Handling Editor: M.P. Cartmell

Keywords:

Passive modeling
Numerical methods
Port-Hamiltonian systems
Multiphysics system
Time domain simulation

ABSTRACT

This paper deals with the time-domain simulation of an electro-mechanical piano: the Fender Rhodes. A simplified description of this multi-physical system is considered. It is composed of a hammer (nonlinear mechanical component), a cantilever beam (linear damped vibrating component) and a pickup (nonlinear magneto-electronic transducer). The approach is to propose a power-balanced formulation of the complete system, from which a guaranteed-passive simulation is derived to generate physically-based realistic sound synthesis.

These issues are addressed in four steps. First, a class of Port-Hamiltonian Systems is introduced: these input-to-output systems fulfill a power balance that can be decomposed into conservative, dissipative and source parts. Second, physical models are proposed for each component and are recast in the port-Hamiltonian formulation. In particular, a finite-dimensional model of the cantilever beam is derived, based on a standard modal decomposition applied to the Euler-Bernoulli model. Third, these systems are interconnected, providing a nonlinear finite-dimensional Port-Hamiltonian System of the piano. Fourth, a passive-guaranteed numerical method is proposed.

This method is built to preserve the power balance in the discrete-time domain, and more precisely, its decomposition structured into conservative, dissipative and source parts. Finally, simulations are performed for a set of physical parameters, based on empirical but realistic values. They provide a variety of audio signals which are perceptively relevant and qualitatively similar to some signals measured on a real instrument.

1. Introduction

Sound synthesis based on physical modeling aims at recovering natural behaviors of existing (or imaginary) instruments. This includes transients, effects due to damping phenomena, timbre variations due to nonlinearities, etc. However, since the models are nonlinear, guaranteeing numerical stability is not straightforward. In this context, approaches based on energy have been developed and applied to simulate musical instruments [1–4]. The principle relies on passivity: conservative (or dissipative) phenomena make the energy time-variation equal to (or lower than) the power received from external sources. Passivity provides energy bounds, from which state bounds stem, so that preserving this property in simulations can be used to address stability issues.

Most of these methods involve space-time discretizations and numerical schemes that are devoted to handle conservative problems and that can successfully be applied to more realistic dissipative models. Technically, these methods are usually designed in

^{*} Corresponding author.

Email address: antoine.falaize@gmail.com (A. Falaize)

¹ The contribution of both authors has been done at IRCAM, Paris, within the context of the French National Research Agency sponsored project HAMECMOPSY. Further information is available at <http://www.hamecmopsys.ens2m.fr>. The PhD thesis of A. Falaize is funded by the EDITE school from Paris.

such a way that a numerical power balance is fulfilled for the discretized quantities (e.g. as the product of discrete velocities and forces). In this paper, this point of view is modified and handled in two steps: (I) derive a passive model in the continuous time-domain, through conservative interconnections of passive elementary components; (II) transpose the complete system in discrete-time domain in such a way that the original power balance is naturally fulfilled and passivity is naturally preserved.

Numerous methods are available to reach step (I). They can be divided in two main classes: (WS) *wave scattering methods* and (KV) *Kirchhoff's variables methods* (see e.g. [5]). Mixed WS/KV methods have also been proposed [6]. Several methods are also available for step (II). *Wave-digital filters* (WDF) [7] and *digital wave-guide* (DWG) [8] are commonly used in audio and acoustic applications. These formalisms belong to the class of WS methods. They allow block-based modeling approaches [6], by introducing links that mimic the serial and parallel connections, and result in passive models for linear systems [9]. WDF and DWG approaches lead to realizable and explicit numerical systems. They are appreciated in real-time sound synthesis applications. However, their benefits are lost for nonlinear systems.

This paper deals with a nonlinear system: the Fender Rhodes piano. Its passive modeling is derived in the class of Port-Hamiltonian Systems, introduced in the 1990s [10–12]. These systems can be considered as an extension of Hamiltonian systems [13] in the sense that these dynamical systems can be composed of conservative components. But they also can include dissipative components as well as some ports connected to external sources and through which energy can transit. These systems admit a power balance that can be decomposed into conservative, dissipative and source parts. They also can be simulated in such a way that the power balance (structured into conservative, dissipative and source parts) is preserved in the discrete-time domain, including for nonlinear systems, see [14], p. 32 and [15]. These modeling and simulation tools are chosen, adapted and used to address the sound synthesis of the Fender Rhodes piano. Preliminary results have been presented in [16].

The paper is organized as follows. In Section 2 the problem statement presents a simplified description of the Rhodes piano and sets the objectives. Section 3 introduces the port-Hamiltonian (pH) formulation. Section 4 is devoted to the physical modeling and the finite-dimensional pH formulation of elementary components. In particular, a finite-dimensional model of an Euler-Bernoulli cantilever beam is derived, based on a standard modal decomposition.

Then, in Section 5, elementary components are connected, yielding the nonlinear finite-dimensional port-Hamiltonian system to simulate (step I). Section 6 details the numerical method that preserves the power balance (step II). Finally, in Section 7, numerical results are presented and some signals are compared to a few measurements.

2. Problem statement

This section describes the Rhodes piano electromechanism. It focuses on the components that are selected to derive the physical model. Then, it states the scientific issues to be addressed to reach guaranteed-passive sound synthesis.

2.1. Overview and main components

A description of the Rhodes piano is given in Fig. 1. The complete system is quite complex (38 components mentioned for each note in Fig. 1©). The resonator is an asymmetric tuning fork (elements 7 to 13 and 19 in Fig. 1©), where one of the prong is called the tine (element 13) and is struck by the hammer (elements 14 and 15), the other prong is called the tone bar (element 11). The constant magnetic induction field due to the pickup magnet in free air is modulated by the movement of the (magnetically conducting) tine, which results in a change of the magnetic flux in the coil, that generates an electromotive force (voltage) from Faraday's law of induction.

This paper focuses on the part depicted in Fig. 1©, from the hammer (excited by a force) to the pickup (producing an output voltage). This part is simplified and modeled by three multi-physical elements (c.f. Fig. 2):

1. a nonlinear hysteretic hammer h , with adjustable material characteristics and geometry,
2. a linear damped cantilever beam b , which can be tuned according to the shape and material properties,

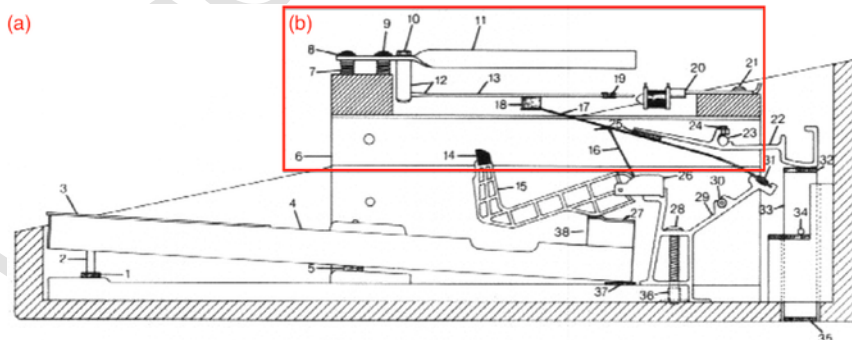


Fig. 1. Overview of a single note of a Rhodes piano: © original schematics [17] (extracted from <http://www.fenderrhodes.com> courtesy of Frederik Adlers); © part selected for modeling.

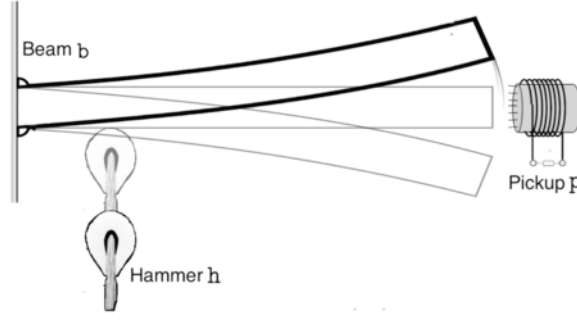


Fig. 2. Schematic of the simplified electromechanical piano, with hammer h , beam b and pickup p .

3. a nonlinear pickup P , the transverse and longitudinal position of which can be adjusted compared to the free-end beam extremity, which is connected to a RC analog filter (not represented in Fig. 2).

This simplification is justified or limited by the following considerations and assumptions. Elements 1–6 and 26–38 are excluded from Fig. 1. They are the body or the key action mechanism. The body is assumed to be ideally rigid. The key action mechanism is ignored in the modeling. Indeed, the exhaust mechanism makes it out of contact with the hammer at the impact time. The hammer (elements 14–15) is then isolated and considered as the excitation part of the proposed model (see [18] for a study on a grand piano). The tuning fork module (elements 7–13 and 19) is the vibrating part of the system. Its modeling is simplified according to the following assumptions:

- (1) The cylindrical tine 13 is modeled as a linear damped Euler-Bernoulli beam.
- (2) The tone bar 11 is neglected, as well as its coupling with the tine through the solid pieces 10 and 12, on which the tine is clamped. Its main role is to store and restore mechanical energy to enhance the sustain. It also has an impact on the transient, the effect of which is not investigated here.
- (3) Elements 7–9 are composed of screws combined with springs with a high stiffness to adjust the transverse position of the tin with respect to the pickup. They are modeled as an ideally rigid connection with the body, located at an adjustable position.
- (4) The fine tuning of the beam is addressed by adjusting the length of the beam rather than including the tuning mass (element 19).

These assumptions are motivated by the following reasons. The linear behavior assumed in (A1) has been validated in [19]. Assumption (A2) is the most critical one in practice, as the tone bar pumps and restores mechanical energy to the tine. It has an impact on the transient and enhances the sustain. These effects are not investigated here in order to simplify the study. Assumptions (A3–A4) correspond to the boundary conditions of a cantilever beam. This allows an exact model order reduction through a decomposition on analytic eigen-functions. The pickup and its placement (elements 20–21) are included in the modeling as they are known to have the main nonlinear impact on the output signal [20]. The damper module (elements 16–18 and 22–25) is ignored in the modeling, meaning that the key release is not taken into account and that the beam is let free until the vibration extinction.

2.2. Objectives

The main objective of this work is to provide a physically-based sound synthesis that generates a large variety of realistic sounds. The second objective is to derive a simulation that preserves fundamental physical principles (causality, stability and, more soundly, passivity and power balance) and that minimizes the computational load. To this end, the following approach is adopted: port-Hamiltonian formulation of the complete system, model order reduction of the infinite dimensional component (beam b), numerical method that preserves the power balance in the discrete-time domain, derivation of a C_{++} code from symbolic calculation to accelerate some costly operations.

3. Port-Hamiltonian systems

This section starts from basic considerations on energy and passivity. It progressively introduces and recalls the *port-Hamiltonian* (pH) formalism [10–12]. It also presents an illustrative example. It is shown how this structure guarantees the passivity of the model in the continuous time-domain.

3.1. Considerations on energy and passivity

Denote $\mathcal{E}(t) \geq 0$ the energy stored in an open physical system. If the system is autonomous and conservative, its time variation $\frac{d\mathcal{E}}{dt}(t)$ is zero. If the system is controlled (non-autonomous) and conservative, $\frac{d\mathcal{E}}{dt}(t)$ is the power $\mathcal{P}_{\text{ext}}(t)$ supplied by sources through

external ports. For systems including dissipative phenomena with dissipated power $\mathcal{Q}(t) \geq 0$, the energy varies according to the *power balance*:

$$\frac{d\mathcal{E}}{dt}(t) = \mathcal{P}_{\text{ext}}(t) - \mathcal{Q}(t). \quad (1)$$

Such systems are passive in the sense that $\frac{d\mathcal{E}}{dt} \leq \mathcal{P}_{\text{ext}}$. In particular, if the sources are not activated, $\frac{d\mathcal{E}}{dt} \leq 0$. The dynamic input-to-output behavior of such a system is the result of the power exchanges between isolated lumped or distributed components. For finite-dimensional systems, those components are sorted as (or can be a combination of): $N_{\mathcal{E}}$ components that store energy $\mathcal{E} \geq 0$ (moving mass, capacitors), $N_{\mathcal{Q}}$ components that dissipate power $\mathcal{Q} \geq 0$ (mechanical damping, transistors), N_{ext} external ports that convey power $\mathcal{P}_{\text{ext}} \in (\mathbb{R})$ from sources (external forces, electrical batteries, etc) or any external system (active, dissipative or mixed). The behavior of each component is described by a relation between two sets of variables: flows \mathbf{f} (velocities, currents, variations of magnetic flux, etc) and their associated efforts \mathbf{e} (forces, voltages, magneto-motive forces, etc). All these quantities are defined in *receiver convention*, where $\mathcal{P} = \mathbf{f}^T \mathbf{e}$ denotes the power *received* by the components.

The energy level of a storage component n depends on an appropriate variable x_n (the elongation $x_n = \ell$ for a spring, the charge $x_n = q$ for a capacitor, the magnetic flux $x_n = \phi$ for a coil, etc). This defines an energy function \mathcal{H}_n ($\mathcal{H}_n(\ell) = (K\ell^2)/2$ for a linear spring with stiffness K , $\mathcal{H}_n(q) = q^2/(2C)$ for a linear capacitor with capacitance C , $\mathcal{H}_n(\phi) = \phi^2/(2L)$ for a linear coil with inductance L , etc). The total stored energy \mathcal{E} is a function \mathcal{H} of the state $\mathbf{x} = [x_1, \dots, x_{N_{\mathcal{E}}}]^T$ given by the sum $\mathcal{E} = \mathcal{H}(\mathbf{x}) = \sum_{n=1}^{N_{\mathcal{E}}} \mathcal{H}_n(x_n)$. The energy variation $\frac{d\mathcal{E}}{dt}$ in (1) is related to the state \mathbf{x} with

$$\frac{d\mathcal{E}}{dt} = \nabla \mathcal{H}(\mathbf{x})^T \frac{d\mathbf{x}}{dt} \quad (2)$$

This variation is precisely the *received power*, that is sum of the products of flows and efforts for all the components $\frac{d\mathcal{E}}{dt} = \mathbf{f}_{\mathcal{E}}^T \mathbf{e}_{\mathcal{E}}$ with $\mathbf{f}_{\mathcal{E}} = [f_1, \dots, f_{N_{\mathcal{E}}}]^T$ and $\mathbf{e}_{\mathcal{E}} = [e_1, \dots, e_{N_{\mathcal{E}}}]^T$ (receiver convention). The external power supplied by sources is the sum of the products of flows and efforts localized at the ports (emitter convention), that is, $\mathcal{P}_{\text{ext}} = \mathbf{f}_{\text{ext}}^T \mathbf{e}_{\text{ext}}$ with $\mathbf{f}_{\text{ext}} = [f_1, \dots, f_{N_{\text{ext}}}]^T$ and $\mathbf{e}_{\text{ext}} = [e_1, \dots, e_{N_{\text{ext}}}]^T$. These flows \mathbf{f}_{ext} and efforts \mathbf{e}_{ext} can be rearranged in two vectors, \mathbf{u} (considered as a system input) and \mathbf{y} (the associated output). This means that $(u_n, y_n) = (f_n, e_n)$ or $(u_n, y_n) = (e_n, f_n)$ for each pair in $(\mathbf{f}_{\text{ext}}, \mathbf{e}_{\text{ext}})$ and yields

$$\mathcal{P}_{\text{ext}} = \mathbf{u}^T \mathbf{y}. \quad (3)$$

Finally, relating the flows and efforts of dissipative components (receiver convention) to the state and port variables, and expressing the total dissipated power as a sum of their product yield

$$\mathcal{Q}(\mathbf{x}, \mathbf{u}) = \left(\nabla \mathcal{H}(\mathbf{x}) \right)^T \mathbf{R} \left(\mathbf{u} \right), \quad (4)$$

the positivity of which is conditioned by that of matrix \mathbf{R} , which can depend on \mathbf{x} (see Section 3.3 for a simple example and Sections 3 and 4 for the Rhodes piano).

3.2. State-space representation of port-Hamiltonian systems

The governing equations of a physical system relate the flows and the efforts introduced above. The port-Hamiltonian systems introduced in [10] (see also [11,12,21]) provide a formulation of such a class of equations for systems that fulfill the power balance (1) with (2)–(4). A differential state-space representation is given by (see e.g. [12], eq 2.53):

$$\underbrace{\begin{pmatrix} \frac{d\mathbf{x}}{dt} \\ -\mathbf{y} \end{pmatrix}}_{\mathbf{b}} = \underbrace{(\mathbf{J}(\mathbf{x}) - \mathbf{R}(\mathbf{x}))}_{\mathbf{M}} \cdot \underbrace{\begin{pmatrix} \nabla \mathcal{H}(\mathbf{x}) \\ \mathbf{u} \end{pmatrix}}_{\mathbf{a}}, \quad (5)$$

where \mathcal{H} is the Hamiltonian, \mathbf{J} is a skew-symmetric matrix ($\mathbf{J}^T = -\mathbf{J}$ for all \mathbf{x}) and \mathbf{R} is a positive semidefinite matrix ($\mathbf{x}^T \mathbf{R} \mathbf{x} \geq 0$ for all \mathbf{x}). The system matrices are structured as follows:

$$\mathbf{J}(\mathbf{x}) = \begin{pmatrix} \mathbf{J}_{\mathbf{x}}(\mathbf{x}) & \mathbf{G}(\mathbf{x}) \\ -\mathbf{G}(\mathbf{x})^T & \mathbf{J}_{\mathbf{y}}(\mathbf{x}) \end{pmatrix}, \quad \mathbf{R}(\mathbf{x}) = \begin{pmatrix} \mathbf{R}_{\mathbf{x}}(\mathbf{x}) & \mathbf{R}_{\mathbf{xy}}(\mathbf{x}) \\ \mathbf{R}_{\mathbf{xy}}(\mathbf{x})^T & \mathbf{R}_{\mathbf{y}}(\mathbf{x}) \end{pmatrix}, \quad (6)$$

with skew-symmetric matrices $\mathbf{J}_{\mathbf{x}} \in \mathbb{R}^{N_{\mathcal{E}} \times N_{\mathcal{E}}}$ and $\mathbf{J}_{\mathbf{y}} \in \mathbb{R}^{N_{\text{ext}} \times N_{\text{ext}}}$, positive semidefinite matrices $\mathbf{R}_{\mathbf{x}} \in \mathbb{R}^{N_{\mathcal{E}} \times N_{\mathcal{E}}}$ and $\mathbf{R}_{\mathbf{y}} \in \mathbb{R}^{N_{\text{ext}} \times N_{\text{ext}}}$, and $\mathbf{R}_{\mathbf{xy}}$ such that \mathbf{R} is positive semidefinite.

As mentioned above, the pH system (5) and (6) fulfills the definition of passivity (see e.g. [22]), according to the following property.

Property 3.1. Power Balance

The variation of the total energy $\mathcal{E} = \mathcal{H}(\mathbf{x})$ of a system governed by (5)–(6) is given by (1), with total incoming power defined in (3) and total dissipated power (4).

Proof

From the above definitions, we have $\mathbf{a}^\top \mathbf{b} = \frac{d\mathcal{E}}{dt} - \mathcal{P}_{\text{ext}}$ and $\mathbf{a}^\top \mathbf{b} = -\mathcal{Q}$ since $\mathbf{a}^\top \mathbf{M} \mathbf{a} = -\left(\frac{\nabla \mathcal{H}(\mathbf{x})}{\mathbf{u}}\right)^\top \mathbf{R} \left(\frac{\nabla \mathcal{H}(\mathbf{x})}{\mathbf{u}}\right)$ from skew-symmetry of \mathbf{J} . \square

Remark 1. Passivity, Lyapunov stability and numerical stability

A main interest of port-Hamiltonian systems is that they satisfy Property 3.1, which ensures Lyapunov stability stemming from passivity. In short, for a state space representation $\frac{d\mathbf{x}}{dt} = \mathbf{f}(\mathbf{x}, \mathbf{u})$, $\mathbf{y} = \mathbf{g}(\mathbf{x}, \mathbf{u})$ (with $\dim(\mathbf{u}) = \dim(\mathbf{y})$) and storage function \mathcal{H} , passivity means that $\frac{d\mathcal{H}(\mathbf{x})}{dt} \leq \mathbf{y}^\top \mathbf{u} = \mathcal{P}_{\text{ext}}$. Property 3.1 ensures this inequality. This implies that if the excitation stops ($\mathbf{u} = 0$ so that $\mathcal{P}_{\text{ext}} = 0$), the storage function \mathcal{H} stops increasing. More precisely, $\mathcal{E} = \mathcal{H}(\mathbf{x})$ is constant in the conservative case ($\mathcal{Q} = 0$) and it decreases in the dissipative case ($\mathcal{Q} > 0$). In these cases, the LaSalle invariance principle states that the trajectory $t \mapsto \mathbf{x}(t)$ tends toward the maximal invariant subspace \mathbb{S} as $t \rightarrow +\infty$, with

$$\mathbb{S} = \{\mathbf{x} \in \mathbb{R}^{N_{\mathcal{E}}} \text{ s.t. } \nabla \mathcal{H}(\mathbf{x})^\top \mathbf{f}(\mathbf{x}, \mathbf{u} = 0) = 0\}. \quad (7)$$

Then, the Lyapunov theorem ensures the system stability as far as \mathcal{H} is positive definite (see also [22], Sections 4.1, 4.2 and 6.2 for details). If \mathcal{H} is not definite, \mathbb{S} provides the set of reachable asymptotic states. This property can be transferred to simulations, using the numerical method presented in Section 6 that preserves the power balance in the discrete time domain.

3.3. Example

In the sequel, for sake of readability, constant values are denoted by capital letters.

Consider the linear mass-spring-damper system depicted in Fig. 3, where gravity is neglected. The mass position is denoted q , with $q = 0$ the spring equilibrium. The system is excited by an external force (f_{ext}).

This system includes $N_{\mathcal{E}} = 2$ storage components, $N_{\text{ext}} = 1$ external port and $N_{\mathcal{Q}} = 1$ dissipative component. The storage components are: mass M with momentum $x_1 = \frac{d(Mq)}{dt}$ and kinetic energy $\mathcal{H}_1(x_1) = x_1^2/(2M)$, and spring K with elongation $x_2 = q$ and potential energy $\mathcal{H}_2(x_2) = (Kx_2^2)/2$. The external port is made of one input $\mathbf{u} = \mathbf{e}_{\text{ext}} = f_{\text{ext}}$ (external force) and one output $\mathbf{y} = \frac{dq}{dt}$. The dissipative component is the damper with dissipated power $\mathcal{Q}_A(\mathbf{x}) = H'_1(x_1)AH'_1(x_1) = A\left(\frac{dq}{dt}\right)^2$. For the mass, $f_M = \frac{dx_1}{dt} = M\frac{d^2q}{dt^2}$ is the fictitious force (effort \mathbf{e}_1) and $\mathcal{H}'_1(x_1) = \frac{dq}{dt}$ is the velocity (flow \mathbf{f}_1). For the spring, $\frac{dx_2}{dt} = \frac{dq}{dt}$ is the velocity (flow \mathbf{f}_2) and $f_K = \mathcal{H}'_2(x_2) = Kq$ is the restoring force (effort \mathbf{e}_2). For the damper, the counteracting force is $f_A = A\frac{dq}{dt}$ so that the associated effort is $\mathbf{e}_A = A\mathcal{H}'_1(x_1)$.

Applying Newton's second law to this simple system yields

$$\begin{pmatrix} \mathbf{e}_1 \\ \mathbf{f}_2 \\ -f_{\text{ext}} \end{pmatrix} = \begin{pmatrix} -A & -1 & +1 \\ +1 & 0 & 0 \\ -1 & 0 & 0 \end{pmatrix} \cdot \begin{pmatrix} \mathbf{f}_1 \\ \mathbf{e}_2 \\ \mathbf{e}_{\text{ext}} \end{pmatrix} \quad (8)$$

From the constitutive laws of components, this equation exactly restores formulation (5) and (6), block by block. This is summarized in Table 1.

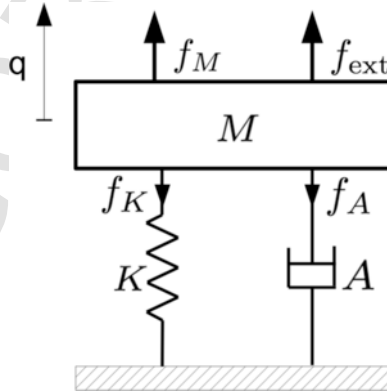


Fig. 3. Damped harmonic oscillator with excitation.

Table 1

Port-Hamiltonian formulation (5) and (6) for the example (8).

State: $\mathbf{x} = (M \frac{dq}{dt}, q)^\top$	Energy: $\mathcal{H}(\mathbf{x}) = \frac{x_1^2}{2M} + \frac{Kx_2^2}{2}$
Input: $\mathbf{u} = f_{\text{ext}}$	Output: $\mathbf{y} = \frac{dq}{dt}$
$\mathbf{J} = \left(\begin{array}{cc c} 0 & -1 & +1 \\ +1 & 0 & 0 \\ -1 & 0 & 0 \end{array} \right), \mathbf{R} = \left(\begin{array}{cc c} A & 0 & 0 \\ 0 & 0 & 0 \\ 0 & 0 & 0 \end{array} \right).$	

4. Models of components

This section presents the multi-physical components that compose each note of a Rhodes piano: (h) a hammer in Section 4.1, (b) a cantilever beam in Section 4.2 and (P) a pickup connected to a RC analog filter in Section 4.3. The hammer h is the nonlinear hysteretic model proposed in [23]. This finite-dimensional system is associated with a non-quadratic energy and a nonlinear damping. The beam b is a linear damped Euler-Bernoulli model [24,25, Section 4.9]. A model order reduction of this infinite-dimensional model is derived, based on a standard modal decomposition. The pickup P is a finite-dimensional nonlinear model [26]. It is composed of one constant magnetic source (magnet), two linear components that stores energy (coil and capacitor), one linear resistor and one electrical port that delivers the output signal (voltage). Contrarily to the hammer, the nonlinearity of the pickup only comes from the magnetic flux induced in the coil by the movement of the beam extremity. The models of these three components prove passive so that they admit port-Hamiltonian formulations.

4.1. Hammer h

The hammer is composed of a rigid core that is covered by a deformable felt. In this paper, its modeling is inspired from that proposed in [23] and used in e.g. [27,28,1] for the acoustic piano. This model describes nonlinear elastic phenomena (see e.g. [29,30] for experimental validations) and nonlinear damping phenomena [31]. This combination yields realistic nonlinear hysteretic effects that account for the shape memory of the felt.

Governing equations. Denote $q_{\text{cont}}(t)$, $q_{\text{core}}(t)$ and L_h , the position of the contact point, the top position of the core and the thickness of the felt at rest, respectively, in an inertial frame of reference (see Fig. 4). For the felt, the crushed thickness is 0 if $q_{\text{core}}(t) + L_h \leq q_{\text{cont}}(t)$ and is

$$q_h(t) = q_{\text{core}}(t) + L_h - q_{\text{cont}}(t) \quad (9)$$

otherwise, so that the crushed rate is given by

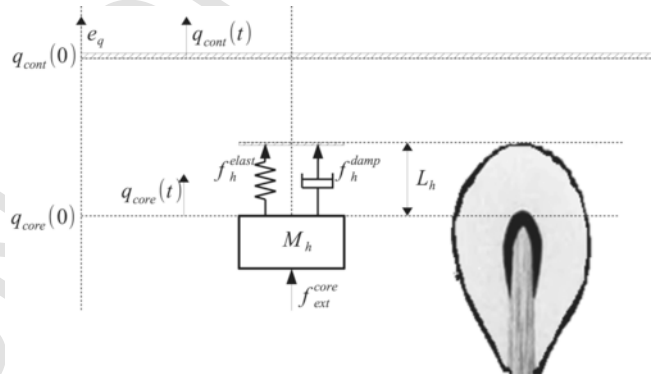


Fig. 4. Mass-spring-damper model of the hammer and notations.

$$c_h(q_h) = \frac{\max(q_h, 0)}{L_h}. \quad (10)$$

The elastic force f_h^{elast} and the damping force f_h^{damp} due to the felt are nonlinear functions of the crush rate given by

$$f_h^{\text{elast}}(c_h) = F_h c_h^{B_h}, f_h^{\text{damp}}(c_h) = A_h L_h \frac{d(c_h^{B_h})}{dt}, \quad (11)$$

where the inertial force of the felt is neglected and parameters are detailed in Table 2. The hammer core can be considered as a mass M_h submitted to the felt force $-(f_h^{\text{elast}} + f_h^{\text{damp}})$ and actuated by an external force $f_{\text{ext}}^{\text{core}}$ (see [18]). Its governing equation is

$$M_h \frac{d^2 q_{\text{core}}}{dt^2} = -f_h^{\text{elast}}(c_h(q_h)) - f_h^{\text{damp}}(c_h(q_h)) + f_{\text{ext}}^{\text{core}}. \quad (12)$$

The mobile contact point with velocity $v_{\text{ext}}^{\text{cont}} = \frac{dq_{\text{cont}}}{dt}$ experiences the reaction force $f_h^{\text{elast}} + f_h^{\text{damp}}$ so that the force exerted by the contact point on the felt is $f_{\text{ext}}^{\text{cont}} = -(f_h^{\text{elast}} + f_h^{\text{damp}})$, and the mechanical power provided to the system is $P_{\text{cont}} = f_{\text{ext}}^{\text{cont}} v_{\text{ext}}^{\text{cont}}$.

Port-Hamiltonian formulation. The port Hamiltonian system of the hammer is derived as in example 3.3. For the mass of the core, the state is the momentum $x_{h,1} = \frac{dM_h q_{\text{core}}}{dt}$ with associated kinetic energy

$$\mathcal{H}_{h,1}(x_{h,1}) = \frac{x_{h,1}^2}{2M_h}. \quad (13)$$

For a spring, the potential energy is given by $\mathcal{H}_{\text{spring}}(q) = \int_0^q f_{\text{spring}}(\xi) d\xi$. In example 3.3, the spring is symmetric and linear ($f_{\text{spring}}(q) = Kq$) so that $\mathcal{H}_{\text{spring}}(q) = Kq^2/2$ is quadratic. For the hammer felt, the spring is non-symmetric (10) and nonlinear (11) so that the associated Hamiltonian $\mathcal{H}_{h,2}$ is a non-even and non-quadratic function of the state $x_{h,2} = q_h$:

$$\mathcal{H}_{h,2}(x_{h,2}) = \frac{L_h F_h}{B_h + 1} c_h(x_{h,2})^{B_h+1}. \quad (14)$$

The flows and efforts of the system are derived as follows. For the mass, $\frac{dx_{h,1}}{dt} = \frac{d^2(M_h q_{\text{core}})}{dt^2}$ is the inertial force (effort labeled $e_{h,1}$) and $\mathcal{H}'_{h,1}(x_{h,1}) = \frac{d}{dt} q_{\text{core}}$ is the velocity (flow labeled $f_{h,1}$). For the spring, $\frac{dx_{h,2}}{dt} = \frac{dq_h}{dt}$ is homogeneous to a velocity (flow $f_{h,2}$) and $\mathcal{H}'_{h,2}(x_{h,2}) = f_h^{\text{elast}}(c_h(q_h))$ is the spring force (effort $e_{h,2}$). For the damper, the damping force is $f_h^{\text{damp}}(q_h) = \frac{A_h L_h}{B_h} c_h(q_h)^{B_h-1} \frac{dq_h}{dt}$ so that the effort is $e^{\text{damp}} = r_h(x_{h,2}) (\mathcal{H}'_{h,1}(x_{h,1}) - v_{\text{ext}}^{\text{cont}})$ with

$$r_h(q_h) = \frac{A_h L_h}{B_h} c_h(q_h)^{B_h-1}. \quad (15)$$

The pH system of the hammer has two external ports. One is associated with the core velocity $\frac{dq_{\text{core}}}{dt}$ (flow $f_{h,3} = f_{h,1}$) and the associated external force $f_{\text{ext}}^{\text{core}}$ (effort $e_{h,3}$). The other one is associated with the contact point velocity $v_{\text{ext}}^{\text{cont}}$ (flow $f_{h,4}$) and the associated external force $f_{\text{ext}}^{\text{cont}}$ (effort $e_{h,4} = -e_{h,2} - e^{\text{damp}}$ so that $f_{h,4} e_{h,4}$ is the power provided by the contact point to the system). Inputs and outputs are chosen to be $\mathbf{u}_h = (e_{h,3}, f_{h,4})$, $\mathbf{y}_h = (f_{h,3}, e_{h,4})$. This choice restores the governing equation (12), summarized in Table 3.

Table 2

Physical parameters for the hammer h. These parameters correspond to typical values found in [30,23] or [32], (I.2.2) with formula $f_h^{\text{elast}} \equiv Ke^p$, $f_h^{\text{damp}} \equiv R \frac{d(e^p)}{dt}$ and $e = L_h c_h$, that is, $p = B_h = 2.5$, $K = L_h^{-B_h} F_h = 5 \times 10^5 \text{ N m}^{-2.5}$ and $R = L_h^{1-B_h} A_h = 100 \text{ N s m}^{-2.5}$.

Label	Description	Typical value	Unit
M_h	Total mass	3×10^{-2}	Kg
L_h	Felt thickness at rest	15×10^{-3}	m
B_h	Felt characteristic exponent	2.5	Dimensionless
F_h	Elastic characteristic force	13.8	N
A_h	Felt damping coefficient	0.184	N s m^{-1}

Table 3

Port-Hamiltonian formulation (5) and (6) for the hammer (see (9) and (13)–(15) for definitions). In this case, the invariant subspace (7) is described by (13) and (14) with (10), that is, $\mathcal{S}_h = \{\mathbf{x}_h \in \mathbb{R}^2 \text{ s.t. } [\mathbf{x}_h]_1 = 0, [\mathbf{x}_h]_2 \leq 0\}$. Inequality $[\mathbf{x}_h]_2 \leq 0$ is due to the fact that the hammer position goes to minus infinity with constant velocity ($[\mathbf{x}_h]_1 = 0$), after it has rebounded on the contact point.

State: $\mathbf{x}_h = \left(\frac{d}{dt}(M_h q_{\text{core}}), q_h\right)^\top$	Energy: $\mathcal{H}_h(\mathbf{x}_h) = \mathcal{H}_{h,1}(x_{h,1}) + \mathcal{H}_{h,2}(x_{h,2})$
Input: $\mathbf{u}_h = (f_{\text{ext}}^{\text{core}}, v_{\text{ext}}^{\text{cont}})^\top$	Output: $\mathbf{y}_h = \left(\frac{d}{dt}q_{\text{core}}, f_{\text{ext}}^{\text{cont}}\right)^\top$
$\mathbf{J} = \left(\begin{array}{cc cc} 0 & -1 & +1 & 0 \\ +1 & 0 & 0 & -1 \\ -1 & 0 & 0 & 0 \\ 0 & +1 & 0 & 0 \end{array} \right), \mathbf{R} = \left(\begin{array}{cc cc} +r_h(x_{h,2}) & 0 & 0 & -r_h(x_{h,2}) \\ 0 & 0 & 0 & 0 \\ 0 & 0 & 0 & 0 \\ -r_h(x_{h,2}) & 0 & 0 & +r_h(x_{h,2}) \end{array} \right).$	

4.2. Beam b

In this paper, the standard Euler-Bernoulli modeling of a damped cantilever beam is used, which results in a linear partial-differential equation (see e.g. [24]). To cope with numerical realizability, we firstly apply a standard modal decomposition and recast the resulting set of ordinary differential equations as a finite dimensional pH system (see [33] and particularly [34, Section 1.3] for infinite dimensional pH description). This contrasts with the finite-element spatial discretization [35] considered in e.g. [1–4].

Euler-Bernoulli modeling. Denoting $z \in (0, L_b)$ the spatial coordinate along the beam, the Euler-Bernoulli modeling [24], [25, Section 4.9] of transverse deflect $q(z, t)$ is

$$M_b \partial_t^2 q + A_b \partial_t q + K_b \partial_z^4 q = f_b \quad (16)$$

where parameters are detailed in Table 4. Initial conditions are $q(z, 0) = 0$ and $\partial_t q(z, 0) = 0$. The configuration space of the deflect q is a Hilbert space $\mathbb{H} = L^2(0, L_b)$. The bounded *inertia operator* and *damping operator* associated with (16) are $\mathcal{M} = M_b \mathcal{I}$ and $\mathcal{C} = A_b \mathcal{I}$, respectively, where \mathcal{I} denotes the identity operator. The *stiffness operator* is $\mathcal{K}q = K_b \partial_z^4 q$ with domain $\mathcal{D}(\mathcal{K}) = \{q \in H^4(0, L_b) \text{ s.t. } q(0) = 0, \partial_z q(0) = 0, \partial_z^2 q(L_b) = 0, \partial_z^3 q(L_b) = 0\}$ (H^4 denotes the standard Sobolev space), that includes the boundary conditions for a cantilever beam, namely: (i) no displacement at the base $q(0, t) = 0$, (ii) no bending at the base $\partial_z q(0, t) = 0$, (iii) no bending moment at the free end $\partial_z^2 q(L_b, t) = 0$, (iv) no shearing force acting at the free end $\partial_z^3 q(L_b, t) = 0$. Operator \mathcal{K} fulfills standard well-posedness properties such as being densely defined, closed, unbounded and self-adjoint on the Hilbert space \mathbb{H} (see [36, Section 2] for technical details, [25, Section 4.9] for the details on the cantilever beam and [37, Section 4 and 5] for a complete functional setting of the Euler-Bernoulli modeling with free ends in the port-Hamiltonian formalism). The total mechani-

Table 4

Fixed and deduced physical parameters for a cylindrical beam b. The moment of inertia of the cross section is given for a cylindrical shape. The length for the desired tone $\omega_b = 2\pi F_b$ is obtain from a numerical evaluation of (18) with $\kappa_m = \sqrt{[4]\omega_m^2 M_b / K_b}$ the dispersion relation.

Label	Description	Typical value	Unit
M_{steel}	Mass density	7750	kg m ⁻³
E_{steel}	Young Modulus	180.10 ⁹	N m ⁻²
R_b	Radius	10 ⁻³	m
A_b	Damping coefficient	5.10 ⁻²	N s ⁻¹
F_b	Tuning frequency	440	Hz
M_b	Mass per unit length	$\pi R_b^2 M_{\text{steel}}$	kg m ⁻¹
I_b	Moment of inertia	$\frac{\pi}{4} R_b^4$	m ⁴
K_b	Flexural rigidity	$E_{\text{steel}} I_b$	N m ²
L_b	Length	5.54.10 ⁻²	m

cal energy is [38, Section 7]:

$$\mathcal{E}_b = \frac{1}{2} \int_0^{L_b} \left(K_b (\partial_z^2 q)^2 + M_b \left(\frac{dq}{dt} \right)^2 \right) dz. \quad (17)$$

Finite dimensional approximation. The linear boundary value problem (16) admits an orthogonal basis of eigenfunctions $B = \{\psi_m\}_{m \in \mathbb{N}_*}$ on the Hilbert space \mathbb{H} . Functions ψ_m are the spatial modes, detailed in Appendix A.1. They satisfy the boundary conditions (i-iv), $\partial_z^4 \psi(z) = \kappa^4 \psi(z)$ for appropriate wave number κ and $\langle \psi_m, \psi_p \rangle = \delta_{m,p}$ (Kronecker's symbol) for all $(m, p) \in \mathbb{N}_*^2$, where the scalar product on \mathbb{H} is defined by $\langle f, g \rangle = \int_0^{L_b} f(z)g(z)dz$. Wave numbers κ_m are the solutions of

$$\cosh(\kappa_m L_b) \cos(\kappa_m L_b) + 1 = 0, \quad (18)$$

with increasing modulus with respect to the index $m \in \mathbb{N}_*$.

The force f_b^{ext} is distributed according to $\sigma_h(z) = \frac{1}{D_b} \mathbf{1}(z - z_h)_{[-D_b/2, D_b/2]}$ and excites all the eigenmodes of the linear model. For the sound synthesis, we are interested by the eigenfrequencies ν_m below the Shannon frequency $\frac{1}{2T}$ (with T the sampling period). Hence, we select the M first modes such that $\nu_M < \frac{1}{2T} < \nu_{M+1}$. Then, we introduce $\mathbf{f} = (f_1, \dots, f_M)^\top = \Omega f_b^{\text{ext}}$ with $\Omega = \langle \sigma_h, \Psi \rangle$ for $\Psi = (\psi_1, \dots, \psi_M)^\top$ (see Appendix A.2). The relations satisfied by the modal displacements $\mathbf{q}_b = \langle q, \Psi \rangle$ are obtained by projecting equation (16) on truncated basis $B_M = \{\psi_m\}_{1 \leq m \leq M}$. This yields the following ordinary differential equations:

$$M_b \frac{d^2 \mathbf{q}_b}{dt^2} + A_b \frac{d \mathbf{q}_b}{dt} + K_b \mathbf{L} \mathbf{q}_b = \mathbf{f} = \Omega f_b^{\text{ext}}, \quad (19)$$

with $\mathbf{L} = \text{diag}(\kappa_1^4, \dots, \kappa_M^4)$, which rewrites $\frac{d \mathbf{x}_b}{dt} = \mathbf{A} \mathbf{x}_b + \mathbf{B} \mathbf{u}_b$ with input $\mathbf{u}_b = f_b^{\text{ext}}$, state $\mathbf{x}_b = \left(\mathbf{q}_b^\top, M_b \frac{d \mathbf{q}_b}{dt}^\top \right)^\top$, $\mathbf{B} = (0, \Omega^\top)^\top$ and

$$\mathbf{A} = \begin{pmatrix} 0 & \frac{1}{M_b} \mathbf{I}_d \\ -K_b \mathbf{L} & -\frac{A_b}{M_b} \mathbf{I}_d \end{pmatrix},$$

where 0 denotes the null matrix and \mathbf{I}_d denotes the identity matrix.

Port-Hamiltonian formulation. The power provided by the external force f_b^{ext} is the product of the later with the collocated velocity v_b^{ext} reconstructed from the modal velocities $v_b^{\text{ext}} = \Omega^\top \frac{d \mathbf{q}_b}{dt}$. This yields to select the output $\mathbf{y}_b = v_b^{\text{ext}} = \mathbf{B}^\top \nabla \mathcal{H}_b$ so that the incoming power is $\mathcal{P} = \mathbf{y}_b^\top \mathbf{u}_b = \int_0^{L_b} \mathbf{y}_b^\top \Psi \Psi^\top \mathbf{u}_b dz$ (with $\mathbf{u}_b = f_b^{\text{ext}}$). From (17) and the modal reconstruction $q = \mathbf{q}_b^\top \Psi$, the total energy of the beam is the Hamiltonian $\mathcal{H}_b(\mathbf{x}_b) = \frac{1}{2} \mathbf{x}_b^\top \mathbf{W} \mathbf{x}_b$, with

$$\mathbf{W} = \begin{pmatrix} K_b \mathbf{L} & 0 \\ 0 & M_b^{-1} \mathbf{I}_d \end{pmatrix}. \quad (20)$$

The resulting port-Hamiltonian system is given in Table 5.

Table 5

Port-Hamiltonian formulation (5) and (6) for the Euler-Bernoulli beam (see (20) for definition of \mathbf{W}). In this case, the invariant subspace (7) is $\mathcal{S}_b = \{0\} \subset \mathbb{R}^{2M}$.

State: $\mathbf{x}_b = (\mathbf{q}_b, M_b \frac{d \mathbf{q}_b}{dt})^\top$	Energy: $\mathcal{H}_b(\mathbf{x}_b) = \frac{1}{2} \mathbf{x}_b^\top \mathbf{W} \mathbf{x}_b$
Input: $\mathbf{u}_b = f_b^{\text{ext}}$	Output: $\mathbf{y}_b = v_b^{\text{ext}}$
$\mathbf{J} = \left(\begin{array}{cc c} 0 & \mathbf{I}_d & 0 \\ -\mathbf{I}_d & 0 & \Omega \\ 0 & -\Omega^\top & 0 \end{array} \right), \mathbf{R} = \left(\begin{array}{cc c} 0 & 0 & 0 \\ 0 & A_b \mathbf{I}_d & 0 \\ 0 & 0 & 0 \end{array} \right).$	

4.3. Pickup P

The electromagnetic pickup P includes a magnet (source of constant magnetic field B_p^{mag}) and a coil with N_{coil} wire turns (sensor for the magnetic field variation). In this paper, the physical modeling of electric guitar pickups [26] is adapted to the system depicted in Fig. 6 (see also the physical model in [39], and physically inspired signal processing modules in [40,41]). In short, a piece of magnetic material (here the beam) changes the spatial distribution of the magnetic field due to the magnet only, hence a change to the flux in the coil ϕ_p . Additionally, the coil is connected to a linear RC circuit, so that its total flux is $\phi_{\text{coil}} = \phi_p + \phi_{\text{RC}}$ with $\frac{d\phi_{\text{RC}}}{dt} = \frac{v_{\text{coil}}}{N_{\text{coil}}}$ (Faraday's law of induction with coil voltage v_{coil}).

First, the coil is modeled as a magnetic capacity in the magnetic domain according to the *gyrator-capacitor* approach [42,43]. Second, we recall the main steps in the derivation of the flux ϕ_p from [26] for the system in Fig. 6. Third, the coil is connected to the RC circuit and the resulting model is recast as a port-Hamiltonian system.

Magneto-electric transducer. According to the gyrator-capacitor approach detailed in [42,43], we adopt the magnetic flux variation $\frac{d\phi}{dt}$ and the magnetomotive force has magnetic flow and effort variables, respectively ($\frac{d\phi}{dt} h \equiv \mathcal{P}$). This permits to model the coil as a linear magnetic capacity: $x_{\text{coil}} = \phi_{\text{coil}}$ and $h_{\text{coil}} = \mathcal{H}'_{\text{coil}}(x_{\text{coil}})$ with $\mathcal{H}_{\text{coil}}(x_{\text{coil}}) = \frac{1}{2C_{\text{coil}}}x_{\text{coil}}^2$. The connection to the electrical domain with v_{coil} the tension and i_{coil} the current trough the coil is obtained from the combination of Ampere's theorem ($h_{\text{coil}} = N_{\text{coil}}i_{\text{coil}}$) and Faraday's law ($v_{\text{coil}} = N_{\text{coil}}\frac{d\phi_{\text{coil}}}{dt}$), yielding a magneto-electric gyrator with ratio $\frac{1}{N_{\text{coil}}}$:

$$\begin{pmatrix} \frac{d\phi_{\text{coil}}}{dt} \equiv \frac{dx_{\text{coil}}}{dt} \\ -i_{\text{coil}} \end{pmatrix} = \begin{pmatrix} 0 & \frac{1}{N_{\text{coil}}} \\ -\frac{1}{N_{\text{coil}}} & 0 \end{pmatrix} \begin{pmatrix} h_{\text{coil}} \equiv \mathcal{H}'_{\text{coil}}(x_{\text{coil}}) \\ v_{\text{coil}} \end{pmatrix}. \quad (21)$$

Notice this connection is conservative: $v_{\text{coil}}i_{\text{coil}} = h_{\text{coil}}\frac{d\phi_{\text{coil}}}{dt}$.

Mechano-magnetic transducer. The two dimensional modeling proposed in [26] for the electric guitar pickup is recalled thereafter. A vibrating sphere with radius A_b (same as the beam) is immersed in a constant magnetic induction field B_p^{mag} due to the magnet. Since there is no conducting current, the total magnetic excitation field is irrotational and derives from a magnetic potential. The magnetization of the sphere with relative magnetic permeability U_{rel} results in an additional term to the potential due to the magnet only. The integration of the total magnetic field over the area bounded by a single wire turn yields the following magnetic flux (see coordinate system and description in Fig. 6):

$$\phi_p = 4B_p^{\text{mag}} R_p^2 \left(4R_p^3 \Delta_U (f_\phi(-(q_p + L_{\text{ver}})) + f_\phi(q_p + L_{\text{ver}})) - 1 \right), \quad (22)$$

$$f_\phi(q_p) = \frac{q_p + R_p}{L_{\text{hor}}^2 + (q_p + R_p)^2}, \quad (23)$$

where $q_p(t)$ is the vertical displacement measured from rest position defined as $(L_{\text{hor}}, L_{\text{ver}})$ and $\Delta_U = \frac{U_{\text{rel}}-1}{U_{\text{rel}}+1}$. The induced tension depends on the flux variation, which reads

$$\frac{d\phi_p}{dt} = f_p\left(q_p, \frac{dq_p}{dt}\right) H_p^{\text{mag}} \quad (24)$$

$$f_p\left(q_p, \frac{dq_p}{dt}\right) = 2a_b^2 U_0 \Delta_U R_p \left(\frac{f_1(q_p) - 2L_{\text{hor}}^2}{f_1^2(q_p)} - \frac{f_2(q_p) - 2L_{\text{hor}}^2}{f_2^2(q_p)} \right) \frac{dq_p}{dt} \quad (25)$$

$$f_1(q_p) = (q_p - R_p + L_{\text{ver}})^2 + L_{\text{hor}}^2, \quad (26)$$

$$f_2(q_p) = (q_p + R_p + L_{\text{ver}})^2 + L_{\text{hor}}^2. \quad (27)$$

Notice the movement of the sphere is not affected by the magnetic field. Finally, the system composed of the magnet, the coil and the moving sphere is modeled as a constant source of magneto-motive force $H_p^{\text{mag}} = \frac{B_p^{\text{mag}}}{U_0}$, connected to a gyrator modulated by the

Table 6

Physical parameters for the pickup P.

Label	Description	Typical value	Unit
B_p	Magnetic field of the magnet	$\pi 4.10^{-7}$	T
U_0	Magnetic permeability of vacuum	$\pi 4.10^{-7}$	H m ⁻¹
U_{steel}	Magnetic permeability of steel	5.10^{-3}	H m ⁻¹
C_{coil}	Magnetic capacity	$3.07.10^{-5}$	H
R_p	Coil radius	5.10^{-3}	m
L_{hor}	Horizontal decay	10^{-2}	m
L_{ver}	Vertical decay	10^{-3}	m
N_{coil}	Number of wire turns	100	Dimensionless
R_{RC}	Electrical resistance	10^3	Ω
C_{RC}	Electrical capacity	33.10^{-8}	F
U_{rel}	Relative magnetic permeability of steel	$\frac{U_{\text{steel}}}{U_0}$	Dimensionless

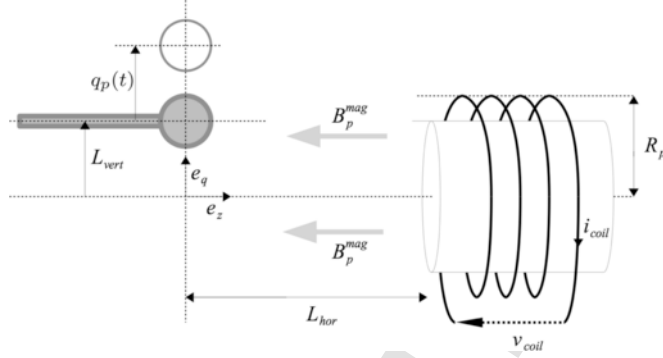


Fig. 6. Description of the pickup. $q_p(t)$ is the position of the end of the beam measured from its rest position, L_{ver} is a vertical decay, q_c is the position of the center of the magnet from the origin of the frame associated with the beam, L_{hor} is the distance between the coil and the beam, $R_p = \frac{a_c^2}{2}$ is the radius of the coil.

$$\begin{cases} [\mathbf{u}_h]_2 &= [\mathbf{y}_b]_1 = (0, \Omega^\top) \nabla \mathcal{H}_b(\mathbf{x}_b), \\ [\mathbf{u}_b]_1 &= -[\mathbf{y}_h]_2 = (r_h(x_{h,2}), 1) \nabla \mathcal{H}_h(\mathbf{x}_h) - r_h(x_{h,2})(0, \Omega^\top) \nabla \mathcal{H}_b(\mathbf{x}_b). \end{cases} \quad (29)$$

Notice this yields a passive interconnection in the sense that the power lost by the hammer is exactly that received by the beam $[\mathbf{u}_b]_1 [\mathbf{y}_b]_1 = -[\mathbf{u}_h]_1 [\mathbf{y}_h]_1$. The connection (29) is then replaced in the diagonal concatenation of structure matrices \mathbf{J} and \mathbf{R} from Tables 3 and 5.

As already stated, the mechanical part is not energetically coupled to the electromagnetic part, and the complete modeling is obtained by concatenating the interconnection (h, b) with the pickup P. The arguments of the modulation coefficient $f_p\left(q_p, \frac{dq_p}{dt}\right)$ (see Table 7) is obtained from the reconstruction of the movement of the beam free end with $q_p = q(L_b)$. Finally, the port-Hamiltonian modeling of the system depicted in Fig. 2 is given in Table 8.

6. Guaranteed passive numerical method

Numerous numerical methods have been developed to simulate dynamical systems governed by $\frac{d\mathbf{x}(t)}{dt} = \mathbf{f}(\mathbf{x}(t), t)$, to approximate the solution $\mathbf{x}(t_k)$, on e.g. a regular grid defined by $t_k = kT$, $k \in \mathbb{Z}$. Many of these methods are based on an approximation of $\frac{d}{dt}$ and exploit the vector field \mathbf{f} at specific instants $t \in [t_k, t_{k+1}]$, but do not preserve passivity. This section introduces a method that preserves the power balance (1) in the discrete time-domain, so that a *numerical power balance* holds:

$$\frac{\mathcal{E}(t_{k+1}) - \mathcal{E}(t_k)}{T} = -\mathcal{Q}(t_k) + \mathcal{P}_{\text{ext}}(t_k). \quad (30)$$

The approach presented below is known as the *discrete gradient method* introduced for classical Hamiltonian systems in [45] (see also [46,47] and [48, Section 4.3]).

6.1. Numerical scheme

Standard first order approximation of the differentials $d\mathbf{x}(t, dt) = \frac{d\mathbf{x}}{dt}(t) \cdot dt$ and $d\mathcal{H}(\mathbf{x}, d\mathbf{x}) = \nabla \mathcal{H}(\mathbf{x})^\top \cdot d\mathbf{x}$ are given by $\delta\mathbf{x}(t_k) = \mathbf{x}(t_{k+1}) - \mathbf{x}(t_k)$, and $\delta\mathcal{H}(\mathbf{x}, \delta\mathbf{x}) = \mathcal{H}(\mathbf{x} + \delta\mathbf{x}) - \mathcal{H}(\mathbf{x}) = \nabla_{\mathcal{H}} \mathcal{H}(\mathbf{x}, \delta\mathbf{x})^\top \cdot \delta\mathbf{x}$, respectively. For mono-variate storage components

Table 8

Port-Hamiltonian formulation (5–6) for the complete system (h, b, p,RC) (see Tables 3, 5 and 7 for definitions), where unspecified matrices are zeros. Here, the invariant subspace (7) is the union of the invariant sets of the components so that $\mathcal{S}_{\text{rhodes}} = \mathcal{S}_h \times \mathcal{S}_b \times \mathcal{S}_p = \{\mathbf{x} \in \mathbb{R}^{2+2+2M} \text{ s.t. } |\mathbf{x}|^2 \leq 0, |\mathbf{x}|_i = 0, i \neq 2\}$, that is, the hammer goes to minus infinity with constant velocity after it has rebounded on the beam, and the latter with pickup circuit return to equilibrium.

State: $\mathbf{x} = (\mathbf{x}_h^\top, \mathbf{x}_b^\top, \mathbf{x}_p^\top)^\top$	Energy: $\mathcal{H}(\mathbf{x}) = \mathcal{H}_h(\mathbf{x}_h) + \mathcal{H}_b(\mathbf{x}_b) + \mathcal{H}_p(\mathbf{x}_p)$
Input: $\mathbf{u} = (f_{\text{ext}}^{\text{core}}, H_p^{\text{mag}}, i_0)^\top$	Output: $\mathbf{y} = (\frac{dq_h}{dt}, \frac{d\phi_0^{\text{mag}}}{dt}, v_0)^\top$
$\mathbf{J}_\mathbf{x} = \begin{pmatrix} 0 & -1 & 0 & 0 & 0 & 0 \\ 1 & 0 & 0 & -\Omega^\top & 0 & 0 \\ 0 & 0 & 0 & \mathbf{I}_d & 0 & 0 \\ 0 & \Omega & -\mathbf{I}_d & 0 & 0 & 0 \\ 0 & 0 & 0 & 0 & 0 & -\frac{1}{N_{\text{coil}}} \\ 0 & 0 & 0 & 0 & \frac{1}{N_{\text{coil}}} & 0 \end{pmatrix}, \mathbf{G} = \begin{pmatrix} 1 & 0 & 0 \\ 0 & 0 & 0 \\ 0 & 0 & 0 \\ 0 & 0 & 0 \\ 0 & f_p(q_p, \frac{dq_p}{dt}) & 0 \\ 0 & 0 & 1 \end{pmatrix},$ $\mathbf{R}_\mathbf{x} = \begin{pmatrix} r_h(x_{h,2}) & 0 & 0 & -r_h(x_{h,2})\Omega^\top & 0 & 0 \\ 0 & 0 & 0 & 0 & 0 & 0 \\ 0 & 0 & 0 & 0 & 0 & 0 \\ -r_h(x_{h,2})\Omega & 0 & 0 & A_b \mathbf{I}_d + \Omega r_h(x_{h,2})\Omega^\top & 0 & 0 \\ 0 & 0 & 0 & 0 & \frac{R_{\text{RC}}}{N^2} & 0 \\ 0 & 0 & 0 & 0 & 0 & 0 \end{pmatrix}.$	

with $\mathcal{H}(\mathbf{x}(t_k)) = \sum_{n=1}^{N_g} \mathcal{H}_n(x_n(t_k))$ (this is the case for the system described in Table 8), a discrete gradient is introduced and defined by

$$[\nabla_d \mathcal{H}(\mathbf{x}(t_k), \delta \mathbf{x}(t_k))]_n = \begin{cases} \frac{\mathcal{H}_n(x_n(t_k) + \delta x_n(t_k)) - \mathcal{H}_n(x_n(t_k))}{\delta x_n(t_k)} & \text{if } \delta x_n(t_k) \neq 0, \\ \mathcal{H}'_n(x_n(t_k)) & \text{otherwise,} \end{cases} \quad (31)$$

so that a discrete chain rule is recovered

$$\frac{\delta \mathcal{E}(t_k)}{T} = \nabla_d \mathcal{H}(\mathbf{x}(t_k), \delta \mathbf{x}(t_k))^\top \frac{\delta \mathbf{x}(t_k)}{T}. \quad (32)$$

Then, applying the following substitution in (5) and (6)

$$\frac{d\mathbf{x}(t_k)}{dt} \rightarrow \frac{\delta \mathbf{x}(t_k)}{T}, \nabla \mathcal{H}(\mathbf{x}(t_k)) \rightarrow \nabla_d \mathcal{H}(\mathbf{x}(t_k), \delta \mathbf{x}(t_k)) \equiv \nabla_d \mathcal{H}_k, \quad (33)$$

leads to

$$\left(\nabla_d \mathcal{H}_k \right)^\top \begin{pmatrix} \frac{\delta \mathbf{x}(t_k)}{\delta t} \\ -\mathbf{y}(t_k) \end{pmatrix} = \underbrace{\nabla_d \mathcal{H}_k^\top \frac{\delta \mathbf{x}(t_k)}{\delta t}}_{\frac{\delta \mathcal{E}(t_k)}{T}} - \underbrace{\mathbf{u}(t_k)^\top \mathbf{y}(t_k)}_{\mathcal{P}_{\text{ext}}(t_k)} = - \underbrace{\left(\nabla_d \mathcal{H}_k \right)^\top \mathbf{R}(\mathbf{x}(t_k)) \begin{pmatrix} \nabla_d \mathcal{H}_k \\ \mathbf{u}(t_k) \end{pmatrix}}_{\mathcal{Q}(t_k)} \quad (34)$$

(same as proof of Property 3.1). For a conservative system ($\mathbf{R} = 0, \mathbf{G} = 0, \mathbf{J}_y = 0$), this method yields $\delta \mathcal{E}(t_k) = 0$ so that $\mathcal{E}(t_{k+1}) = \mathcal{E}(t_k)$ (the energy is conserved). For a passive system ($\mathbf{R} \neq 0, \mathbf{G} \neq 0, \mathbf{J}_y \neq 0$), this method restores a discrete version of Property 3.1 so that observations of Remark 1 holds. Notice the invariant set $\mathcal{S}_{\text{rhodes}}$ is the same as in the continuous time domain (see caption of Table 8).

The associated update is

$$\mathbf{x}(t_{k+1}) = \mathbf{x}(t_k) + \delta \mathbf{x}(t_k), \quad (35)$$

$$\delta \mathbf{x}(t_k) = T (\mathbf{J}_x - \mathbf{R}_x) \nabla_d \mathcal{H}(\mathbf{x}(t_k), \delta \mathbf{x}(t_k)) + T (\mathbf{G} - \mathbf{R}_{xy}) \mathbf{u}(t_k), \quad (36)$$

$$\mathbf{y}(t_k) = (\mathbf{G} + \mathbf{R}_{xy})^\top \nabla_d \mathcal{H}(\mathbf{x}(t_k), \delta \mathbf{x}(t_k)) - (\mathbf{J}_y - \mathbf{R}_y) \mathbf{u}(t_k) \quad (37)$$

where state-dependent matrices are evaluated at $\mathbf{x}(t_k)$, and the implicit relation on $\delta \mathbf{x}(t_k)$ is solved at each time step by a fixed number of Newton-Raphson iterations. Notice the Rhodes model in Table 8 includes a single nonlinear storage component (spring effect associated with the hammer felt). In this case, the Newton-Raphson algorithm only requires the inversion of a scalar function, that allows real-time applications.

6.2. Convergence analysis

Although the discrete power balance ensures the asymptotic stability of the numerical solution, it does not provide information on the convergence of the sequence $\mathbf{x}(t_k)$ to the continuous solution. From Lax's theorem, convergence holds provided (i) the method is consistent with the system (5) and (6) and (ii) the total error can be bounded (stability of the method). From [49, (3), Section 4.2], the method that yields the slope $\sigma(t_k) = \frac{\delta \mathbf{x}_k}{T}$ is consistent if and only if

$$\lim_{T \rightarrow 0} \sigma(t_k, T) = \mathbf{f}(\mathbf{x}(t_k), t_k). \quad (38)$$

Assuming that \mathcal{H} satisfies a Lipschitz condition (this is the case for the system in Table 8), the discrete gradient is consistent with the continuous gradient:

$$\lim_{\|\delta \mathbf{x}\|_2 \rightarrow 0} \nabla_d \mathcal{H}(\mathbf{x}, \delta \mathbf{x}) = \nabla \mathcal{H}(\mathbf{x}). \quad (39)$$

Now, provided the structure matrices $\mathbf{J}(\mathbf{x})$ and $\mathbf{R}(\mathbf{x})$ are bounded (this is the case for the system in Table 8), the slope $\sigma(t_k)$ is bounded so that $\lim_{T \rightarrow 0} \delta \mathbf{x}(t_k) = 0$. This proves the numerical method is consistent up to order 1. Additionally, the method (33) proves *stable* (in the sense that the total error due to the accumulation of round-off and truncation errors is bounded) from the Lipschitz property of the Hamiltonian \mathcal{H} and the structure matrices (see [49, theorem 4.1]). This proves the convergence of the discrete gradient method for port-Hamiltonian systems (5) and (6).

Remark 2. Second order

Order 2 is achieved for constant matrices \mathbf{J} and \mathbf{R} , and can be recovered for non constant structure with an additional computation step of Runge-Kutta type (see [15] for details).

Remark 3. Coincidence with the midpoint rule

For port-Hamiltonian systems composed of a collection of linear energy storing components with quadratic Hamiltonian $\mathcal{H}_n(x_n) = \frac{x_n^2}{2C_n}$, we define $\mathbf{Q} = \text{diag}(C_1 \cdots C_{N_g})^{-1}$ so that the discrete gradient (31) reads

$$\nabla_d \mathcal{H}(\mathbf{x}, \mathbf{x} + \delta \mathbf{x}) = \mathbf{Q} \left(\mathbf{x}(k) + \frac{\delta \mathbf{x}(k)}{2} \right). \quad (40)$$

For a constant structure, this restores the midpoint rule $\frac{\delta \mathbf{x}_k}{T} = \mathbf{f} \left(\frac{\mathbf{x}_k + \mathbf{x}_{k+1}}{2} \right)$ that coincides in this case with the trapezoidal rule $\frac{\delta \mathbf{x}_k}{T} = \frac{\mathbf{f}(\mathbf{x}_k) + \mathbf{f}(\mathbf{x}_{k+1})}{2}$. However, for nonlinear cases, (31) leads to a class of numerical schemes depending on the nonlinearity, still preserving passivity. In these cases, the discrete gradient approach does not coincide anymore with the midpoint rule, which also does not coincide anymore with the trapezoidal rule.

7. Results

In this section, the numerical scheme (33) is applied on the modeling presented in Section 5. The sample rate is $T^{-1} = 48$ kHz. Physical parameters are given in Tables 2, 4 and 6. They are chosen to correspond to the musical note A4 (440 Hz). The basis of eigenmodes is truncated so that the highest eigenfrequency is below the Nyquist frequency, which yields $M=4$ modes for note A4 at 48 kHz. The corresponding eigenfrequencies are $\nu_1 = 440$ Hz, $\nu_2 \simeq 2757.49$ Hz, $\nu_3 \simeq 7721.07$ Hz and $\nu_4 \simeq 15130.22$ Hz (see Section 4.2 and Appendix A.1). Audio example are available here.² The input force $f_{\text{ext}}^{\text{core}}$ is comprised between 0 and 10^3 N, during 1 ms. A simple exhaust mechanism is included (not shown in Tables 3 and 8) with $f_{\text{ext}}^{\text{core}} = 0$ if $q_h > -0.5$ cm.

² <http://recherche.ircam.fr/anasy/falaize/applis/rhodes/index.html>

7.1. Mechanical energy

The dynamics of the hammer is shown in Fig. 7 for $f_{\text{ext}}^{\text{core}} = 500$ N. We see it accelerates between 1ms and 2ms and impacts the beam at $t_i \simeq 2.5$ ms. During the impact, a part of the energy transferred from the hammer to the beam is dissipated (see Fig. 8a). The energy in the beam is shown in Fig. 8b. We see that a numerical energy balance is fulfilled.

7.2. Electromagnetic energy

The source of constant magnetomotive force is modulated according to Section 4.3. Note such a source can be locally a sink of power, as seen in Fig. 9 where the power passes slightly under 0 W. Again, the numerical error on the power balance is close to the machine epsilon.

7.3. Output signal

The output voltage v_0 is proportional to the beam free-end velocity multiplied by a nonlinear function of the position $q_p = q(z = L_b)$ given by (25). Since the beam modeling is linear (see Section 4.2), this transduction mechanism is the only one that is responsible for the characteristic Rhodes piano tones, as noticed in [19,20]. Fig. 10 displays the displacement and the velocity of the beam free-end as well as the output voltage v_0 (see Fig. 5 and Tables 7 and 8). These signals have been computed for $f_{\text{ext}}^{\text{core}} = 500$ N (note A4). We can notice in Fig. 10b that higher modes of the resonator are not extensively excited, and that the distinctive evolution of the tone is due to the pickup only.

7.4. Comparison with measurements

The physical modeling approach to sound synthesis provides an easy tuning of the model parameters to simulate a given device. This has been done based on measurements provided by UVI,³ a company specialized in building sample-based real-time synthesizers of musical instruments. A rough comparison of spectrograms for increasing hammer force (from 100 N to 1000 N in the pH model) is shown in Fig. 11. A detailed comparison of the normalized waveforms in the cases force 1, force 4 and force 7 is given in Fig. 12.

7.5. Playing with the model

According to the Fender Rhodes manual, the position of the pickup with respect to the beam's axis has a critical effect on the resulting timbre and transients of the output voltage. This can be easily verified in our simulations. Results for the horizontal L_{hor} and vertical alignment L_{ver} prove in good accordance with predicted behaviors as shown in Figs. 13.

8. Conclusions

In this paper, a nonlinear finite-dimensional model of a simplified electro-mechanical piano has been developed, based on a set of elementary components (hammer, beam and pickup), in the framework of port Hamiltonian systems. This formalism splits the system into conservative, dissipative and source parts. A numerical method has been derived, which preserves this decomposition and the power balance in the discrete time domain. The analysis of numerical results proves the relevancy of the method: first, the analysis of the power exchanges and of the total energy shows that passivity is fulfilled; second, the numerical scheme proves compatible with real-time purposes; third, results are consistent with measurements on a real device.

Several model sophistications and refinements could be considered in perspectives of this work, some of which are listed thereafter in order of importance with respect to the sound realism. First of all is the modeling of both prongs for the resonator (elements 7–13 in Fig. 1) with their energy transfer. This should directly impact the transient and damping of output signal, as pointed out in [19]. Another critical element for playing with the instrument is the damper module (elements 16–18 and 22–25 in Fig. 1), which permits to control the duration of the vibration. The modeling of the hammer felt can be reused to address this issue. A less critical refinement is concerned with the movement of the tine that is not perfectly planar, thus inducing polarization effects that can appear in the output signal. This leads to consider a three-dimensional model for the tine vibration, and to adapt the pickup model accordingly. Additionally, the shear stress due to the deflect of the tine should be included; it does not seem to be necessary to describe torsion nor compression waves, due to (i) the filiform geometry and (ii) the axial excitation mechanism. The hammer model could be complemented by modeling the key action mechanism (see [50] and references therein), and the hammer felt model could be refined so as to exhibit a realistic asymptotic behavior (that is, the felt can not be infinitely crushed). Least of all, the mechano-electric transducer could be refined to include the energetic exchange due to the coupling between the beam and the magnetic field,

³ <http://www.uvi.net/>

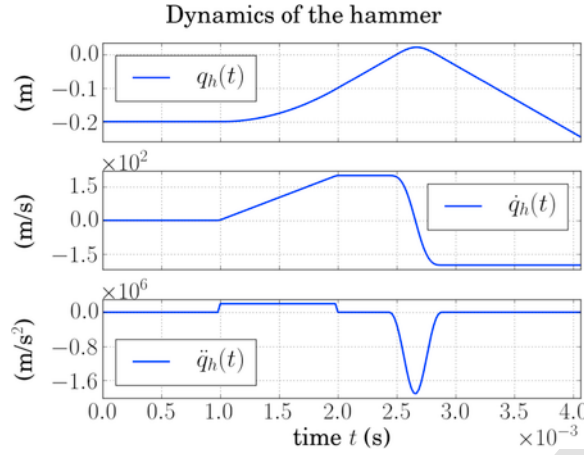


Fig. 7. Position, velocity and acceleration of the hammer.

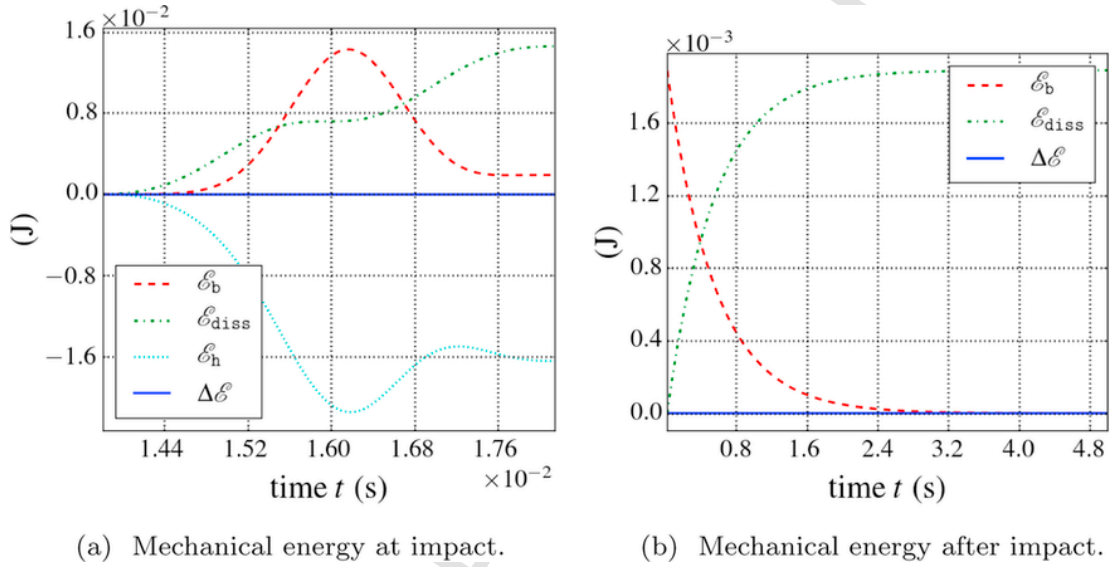


Fig. 8. Evolution of the mechanical energy. \mathcal{E}_b is the energy of the beam, \mathcal{E}_{diss} is the dissipated energy $\int \mathcal{Q} dt$, \mathcal{E}_h is the increment on the energy of the hammer $\mathcal{H}_h(\mathbf{x}_h(t)) - \mathcal{H}_h(\mathbf{x}_h(t_0))$ with t_0 the impact moment and $\Delta \mathcal{E}$ is the energy balance $\mathcal{E}_b + \mathcal{E}_h + \mathcal{E}_{diss}$.

by considering the Maxwell force. This should not alter the output signal except for increasing the damping; this point is to consider only in view of a comprehensive multi-physical model.

A second perspective is to look for a method to extract the physical parameters from the measurements, in order to increase the sound realism. A third perspective is to examine second order explicit numerical schemes (see e.g. [15]) to improve accuracy and reduce the computational cost. Finally, a playable instrument plugin could be developed based on C++ implementation.

Acknowledgments

The authors acknowledge the members of the French National Research Agency project HaMecMoPSys for support in port-Hamiltonian theory, Cyril Touz   for lectures on modal decomposition and UVI company (especially Damien Vallet) for providing high quality measurement of Rhodes tones. Last but not least, the authors acknowledge David Roze for careful proofreading.

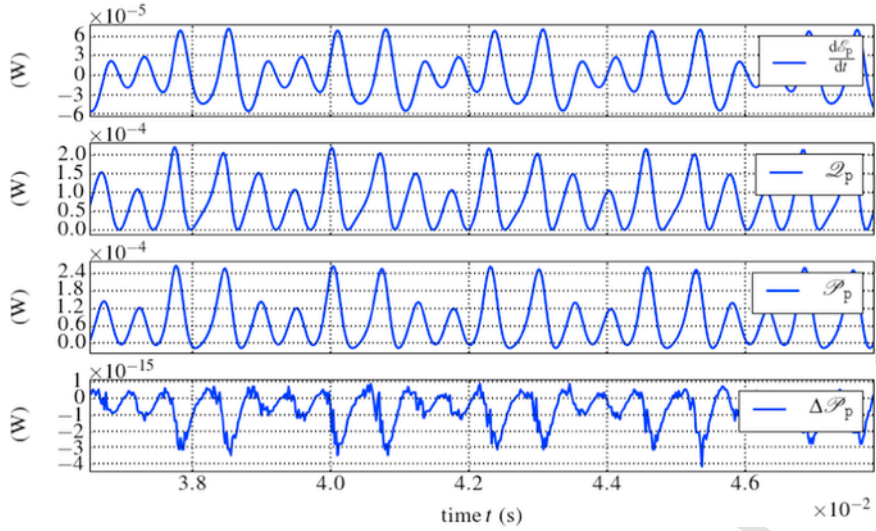
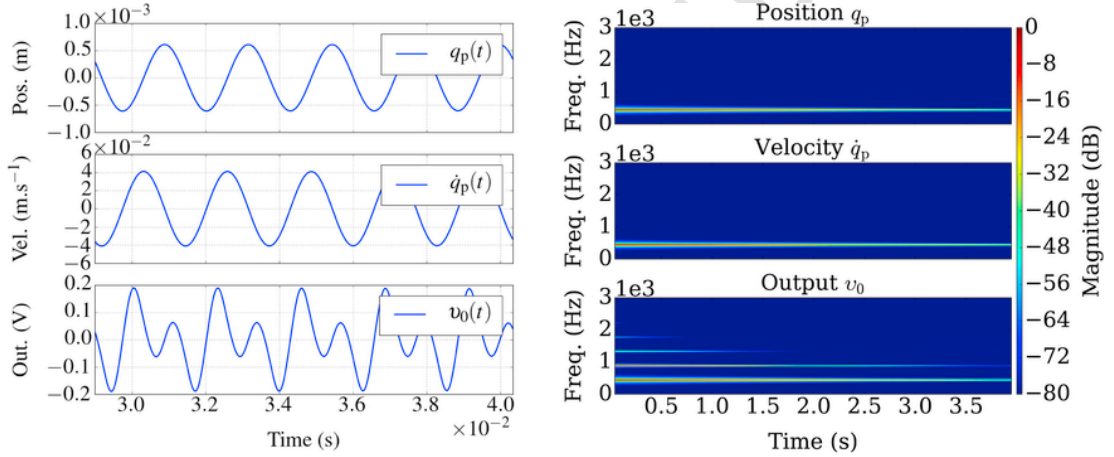


Fig. 9. (Simulation) Power balance for the electro-magnetic part (pickup and RC analog circuit) with energy variation $\frac{d\epsilon_p}{dt} = \nabla \mathcal{H}_p^T \frac{dx_p}{dt}$, dissipated power $\mathcal{Q}_p = \frac{R_{RC}}{N_{coil}^2} [\nabla \mathcal{H}_p]^2$, source power $\mathcal{P}_p = \mathbf{u}_p^T \mathbf{y}_p$ (see Table 7), and deviation on the power balance $\Delta \mathcal{P}_p = \left(\frac{d\epsilon_p}{dt} + \mathcal{Q}_p - \mathcal{P}_p \right) / \langle \mathcal{P}_p \rangle$, relative to the mean source power $\langle \mathcal{P}_p \rangle \simeq 10^{-4}$ W for the five periods shown in the figure.



(a) Reconstruction of beam displacement and velocity at the beam free end $z = L_b$, and output voltage v_0 . (b) Normalized spectra obtained from fast Fourier transform on 2^{11} samples with overlap ratio 50%.

Fig. 10. (Simulation) Displacement $q_p = q(z = L_b)$ and velocity $\frac{dq_p}{dt}$ of the free end of the beam, and corresponding output voltage v_0 that results from the pickup non-linearity (25).

Appendix A. Modal decomposition

A.1. Orthonormal basis

The spatial eigenvectors $\psi_m(z)$ which satisfy the boundary conditions of the cantilever beam (i-iv), $\partial_z^4 \psi(z) = \kappa^4 \psi(z)$ and $\langle \psi_m, \psi_p \rangle = \delta_{m,p}$ (Kronecker's symbol) for all $(m, p) \in \mathbb{N}_*^2$, where the scalar product on $L^2(0, L_b)$ is defined by $\langle f, g \rangle = \int_0^{L_b} f(z)g(z)dz$ are

$$\psi_m(z) = \gamma_m \hat{\psi}_m(z) \hat{\psi}_m(z) = \theta_m (\sin \kappa_m z - \sinh \kappa_m z) + \cos \kappa_m z - \cosh \kappa_m z \quad (\text{A.1})$$

for the normalizing coefficient

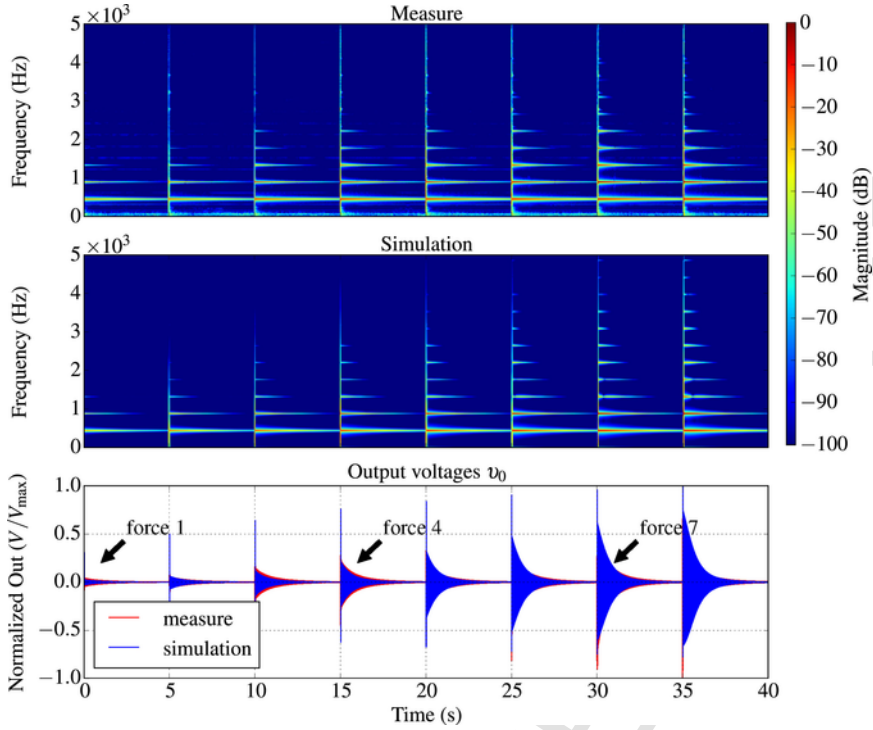


Fig. 11. Spectral densities for the reference (upper) and simulation (middle), and normalized output voltages (lower). See Fig. 12 for a detailed comparison of waveforms in the cases force 1, force 4 and force 7. The dynamics for the spectrograms is 100 dB, which is perceptively relevant for audio applications. We see the recorder tones (upper) exhibits additional spectral content, mostly on the band [1–2] kHz. This could come from the double polarization of the beam movement or from the coupling with the tone bar, that are not taken into account in the proposed model. The low frequency content is associated with external noise induced in the recorded signals. Finally, we see the model could benefit from an eigenmode dependent damping coefficient $A_b \equiv [A_{b,m}]_{1 \leq m \leq M}$ to fit with the decay of partials in the recorded tones.

$$\gamma_m = \left(\frac{\kappa_m L_b (\cos 2\kappa_m L_b + \cosh 2\kappa_m L_b - 2)}{2\kappa_m (\cos \kappa_m L_b + \cosh \kappa_m L_b)^2} \frac{\cosh \kappa_m L_b (2 \sin \kappa_m L_b + \cosh \kappa_m L_b \sin 2\kappa_m L_b)}{2\kappa_m (\cos \kappa_m L_b + \cosh \kappa_m L_b)^2} \right)^{1/2}, \quad (\text{A.2})$$

with $\cos(\kappa_m L_b) \cosh \kappa_m L_b + 1 = 0$ and $\theta_m = \frac{\sin(\kappa_m L_b) - \sinh(\kappa_m L_b)}{\cos(\kappa_m L_b) + \cosh(\kappa_m L_b)}$.

A.2. Projection

The projection of a point force f_b^{ext} located at z_h and distributed according to $\sigma_h(z) = 1(z - z_h)_{[-D_h/2, +D_h/2]}$ on the truncated basis $B = \{\psi_m\}_{1 \leq m \leq M}$ is Ωf_b^{ext} with

$$a_m = \sqrt{\frac{2}{\kappa_m}} \left[2 \sin \left(C_h \frac{\kappa_m}{2} \right) \left(\cos(\kappa_m (L_b - z_h)) + \cos(\kappa_m z_h) \cosh(\kappa_m L_b) - \sin(\kappa_m z_h) \sinh(\kappa_m L_b) \right) - 2 \sinh \left(C_h \frac{\kappa_m}{2} \right) \right]$$

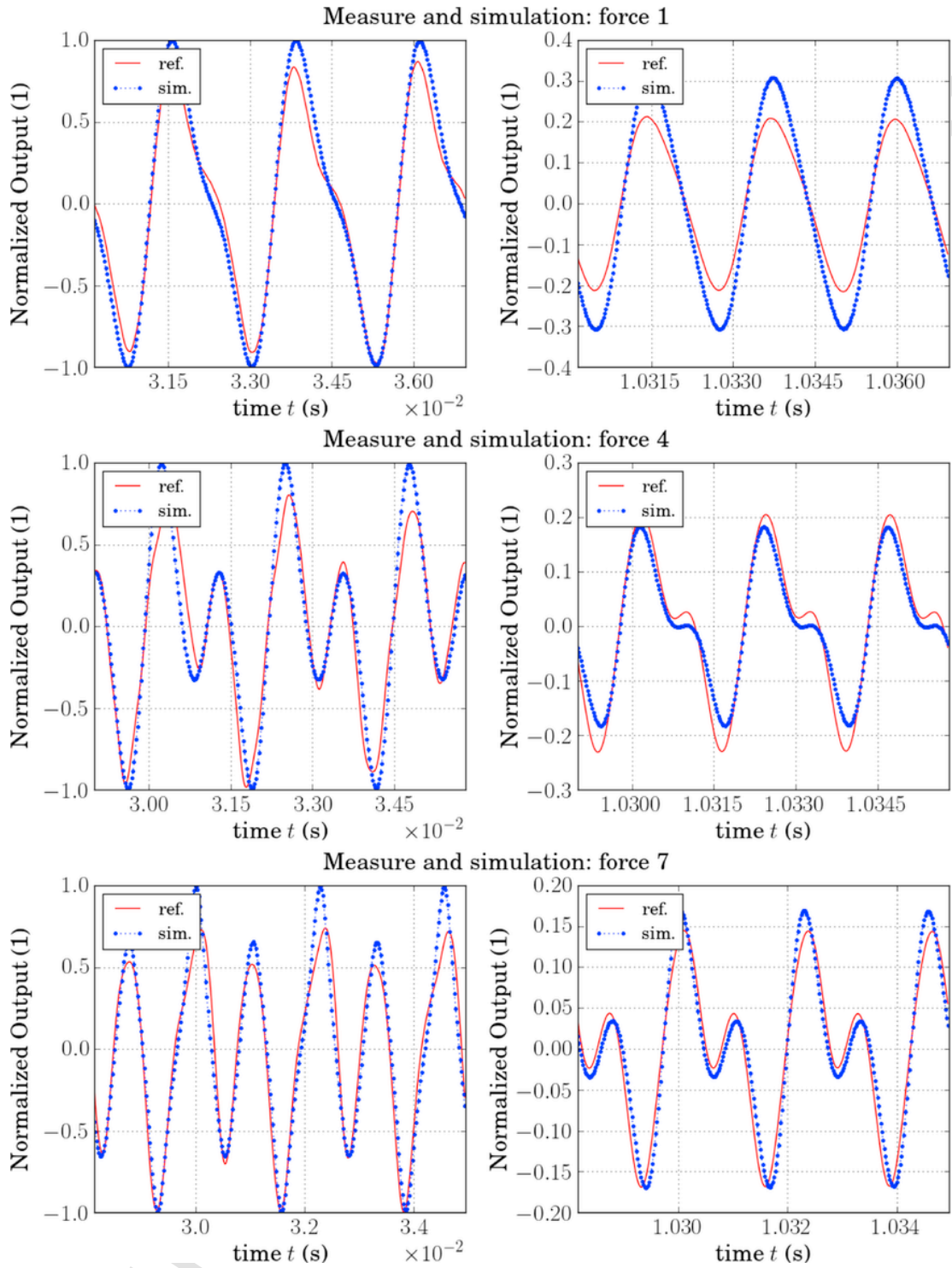


Fig. 12. Comparison with reference signals (see Fig. 11 for correspondence of forces).

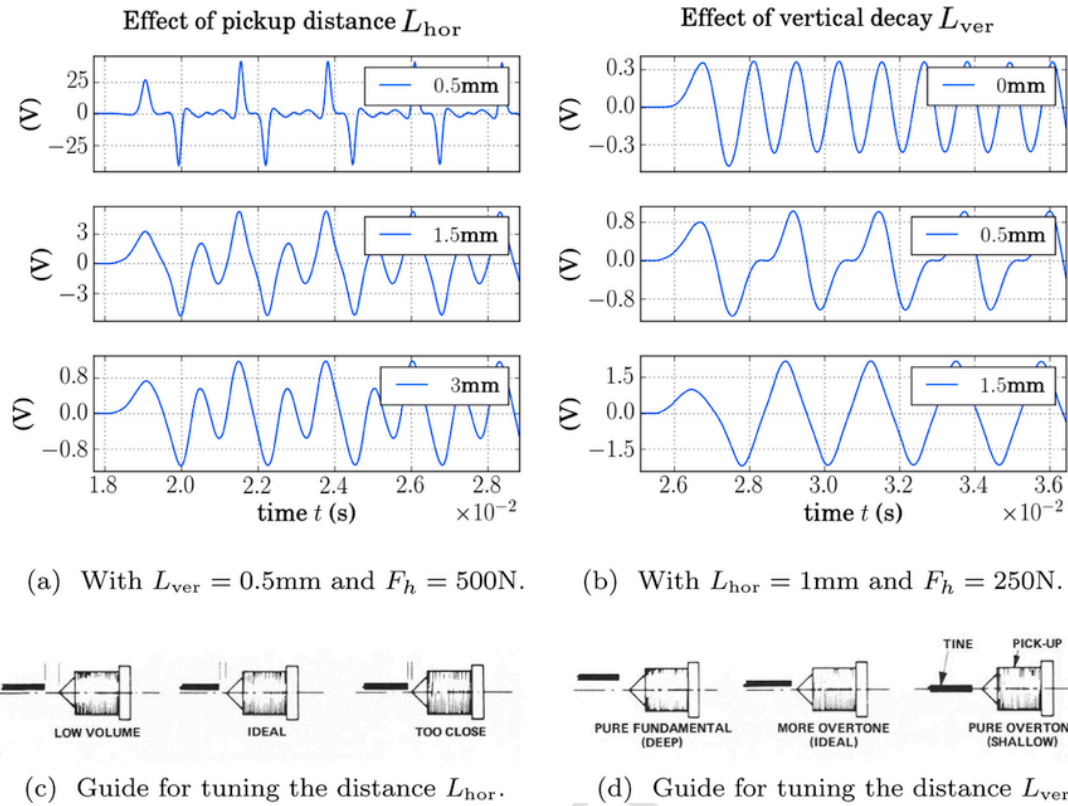


Fig. 13. Effect of vertical alignment L_{ver} and horizontal distance L_{hor} on the output signal v_o .

References

- [1] J. Chabassier, A. Chaigne, P. Joly, Modeling and simulation of a grand piano, *J. Acoust. Soc. Am.* 134 (1) (2013) 648–665.
- [2] C. Desvages, S. Bilbao, Physical modeling of nonlinear player-string interactions in bowed string sound synthesis using finite difference methods, in: *Proceedings of the International Symposium on Musical Acoustics*, 2014.
- [3] S. Bilbao, A. Torin, Numerical simulation of string/barrier collisions: The fretboard, in: *Proceedings of the 17th International Conference on Digital Audio Effects (DAFx-14)*, 2014.
- [4] S. Bilbao, A. Torin, V. Chatzioannou, Numerical modeling of collisions in musical instruments, *Acta Acust. U. Acust.* 101 (1) (2015) 155–173.
- [5] V. V  lim  ki, J. Pakarinen, C. Erkut, M. Karjalainen, Discrete-time modelling of musical instruments, *Reports on progress in physics* 69.
- [6] S. Petrausch, Block based physical modeling, (Ph.D. thesis), Ph. D. dissertation, University of Erlangen Nuremberg, 2007.
- [7] A. Fettweis, Wave digital filters: theory and practice, *Proc. IEEE* 74 (2) (1986) 270–327.
- [8] J.O. Smith, Physical modeling using digital waveguides, *Comput. Music J.* (1992) 74–91.
- [9] A. Fettweis, Pseudo-passivity, sensitivity, and stability of wave digital filters, *IEEE Trans. Circuit Theory* 19 (6) (1972) 668–673.
- [10] B. Maschke, A.J. Van Der Schaft, P.C. Breedveld, An intrinsic hamiltonian formulation of network dynamics: non-standard poisson structures and gyrators, *J. Frankl. Inst.* 329 (5) (1992) 923–966.
- [11] A. van der Schaft, Port-Hamiltonian systems: an introductory survey, in: *Proceedings of the International Congress of Mathematicians, Madrid, August 22–30, 2006*, 2006, pp. 1339–1365.
- [12] V. Duindam, A. Macchelli, S. Stramigioli, H. Bruyninckx, *Modeling and Control of Complex Physical Systems: the Port-Hamiltonian Approach*, Springer Science & Business Media, 2009.
- [13] J.E. Marsden, T. Ratiu, *Introduction to Mechanics and Symmetry: a Basic Exposition of Classical Mechanical systems*, 17, Springer Science & Business Media, 2013.
- [14] S. Aoues, Sch  mas d'int  gration d  di  s    l'  tude, l'analyse et la synth  se dans le formalisme hamiltonien    ports, (Ph.D. thesis), INSA de Lyon, 2014.
- [15] N. Lopes, T. H  lie, A. Falaize, Explicit second-order accurate method for the passive guaranteed simulation of port-Hamiltonian systems, in: *Proceedings of the 5th IFAC Workshop on Lagrangian and Hamiltonian Methods for Non Linear Control (Lyon, France)*, 2015.
- [16] A. Falaize, T. H  lie, Guaranteed-passive simulation of an electro-mechanical piano: A port-hamiltonian approach, in: *Proceedings of the 18th International Conference on Digital Audio Effects (DAFx-15)*, 2015.
- [17] R.K. Instruments, Service Manual, CBS Musical Instruments, a division of CBS Inc., California, USA, 1979. <<http://www.fenderrhodes.com/>>.
- [18] H.C. Hart, M.W. Fuller, W.S. Lusby, A precision study of piano touch and tone, *J. Acoust. Soc. Am.* 6 (2) (1934) 80–94.
- [19] M. Muenster, F. Pfeifle, T. Weinrich, M. Keil, Nonlinearities and self-organization in the sound production of the rhodes piano, *J. Acoust. Soc. Am.* 136 (4) (2014). (2164–2164).
- [20] M. Muenster, F. Pfeifle, Non-linear behaviour in sound production of the rhodes piano, in: *Proceedings of the International Symposium of Musical Acoustics (ISMA)*.
- [21] A. van der Schaft, D. Jeltsema, *Port-Hamiltonian Systems Theory: an Introductory Overview*, Now Publishers Inc., 2014.
- [22] H.K. Khalil, J. Grizzle, *Nonlinear Systems*, 3, Prentice hall, New Jersey, 1996.
- [23] A. Stulov, Experimental and theoretical studies of piano hammer, in: *Proceedings of the Stockholm Music Acoustics Conference*, 2003.
- [24] K.F. Graff, *Wave Motion in Elastic Solids*, Dover publication, New York, 1973.

- [25] S.G. Kelly, *Advanced Vibration Analysis*, CRC Press, 2006.
- [26] K.T. McDonald, Electric guitar pickups, in: Pedagogic note, Princeton University, Department of Physics, 2007, <<http://puhep1.princeton.edu/~mcdonald/examples/guitar.pdf>>.
- [27] N.H. Fletcher, T.D. Rossing, *The Physics of Musical Instruments*, Springer Science & Business Media, 1998.
- [28] N. Giordano, J. Winans II, Piano hammers and their force compression characteristics: does a power law make sense?, *J. Acoust. Soc. Am.* 107 (4) (2000) 2248–2255.
- [29] M. Ghosh, Experimental study of the duration of contact of an elastic hammer striking a damped pianoforte string.
- [30] X. Boutillon, Model for piano hammers: experimental determination and digital simulation, *J. Acoust. Soc. Am.* 83 (2) (1988) 746–754.
- [31] A. Stulov, Hysteretic model of the grand piano hammer felt, *J. Acoust. Soc. Am.* 97 (4) (1995) 2577–2585.
- [32] J. Chabassier, *Modélisation et simulation numérique d'un piano par modèles physiques*, (Ph.D. thesis), Ecole Polytechnique X, 2012.
- [33] A. Macchelli, C. Melchiorri, Modeling and control of the timoshenko beam. The distributed port hamiltonian approach, *SIAM J. Control Optim.* 43 (2) (2004) 743–767.
- [34] J.A. Villegas, *A port-Hamiltonian approach to distributed parameter systems*, (Ph.D. thesis), 2007.
- [35] V. Chatzioannou, M. Van Walstijn, An energy conserving finite difference scheme for simulation of collisions, in: *Proceedings of the sound and music computing conference (SMC2013)*, Stockholm, 2013, pp. 584–591.
- [36] R.F. Curtain, H. Zwart, *An Introduction to Infinite-Dimensional Linear Systems Theory*, 21, Springer Science & Business Media, 2012.
- [37] T. Hélie, D. Matignon, Nonlinear damping models for linear conservative mechanical systems with preserved eigenspaces: a port-hamiltonian formulation, *IFAC-Paper Online* 48 (13) (2015) 200–205.
- [38] L. Meirovitch, *Principles and Techniques of Vibrations*, 1, Prentice Hall, New Jersey, 1997.
- [39] N.G. Horton, T.R. Moore, Modeling the magnetic pickup of an electric guitar, *Am. J. Phys.* 77 (2) (2009) 144–150.
- [40] R.C. Paiva, J. Pakarinen, V. Välimäki, Acoustics and modeling of pickups, *J. Audio Eng. Soc.* 60 (10) (2012) 768–782.
- [41] L. Remaggi, L. Gabrielli, R.C.D. de Paiva, V. Välimäki, S. Squartini, A pickup model for the clavinet, in: *Digital Audio Effects Conference (DAFx-12)*, 2012.
- [42] D.C. Hamill, Lumped equivalent circuits of magnetic components: the gyrator-capacitor approach, *IEEE Trans. Power Electron.* 8 (2) (1993) 97–103.
- [43] D.C. Hamill, Gyrator-capacitor modeling: a better way of understanding magnetic components, in: *Proceedings of the Applied Power Electronics Conference and Exposition (APEC'94)*, Ninth Annual, IEEE, 1994, pp. 326–332.
- [44] J. Cervera, A. Van Der Schaft, A. Baños, Interconnection of port-Hamiltonian systems and composition of Dirac structures, *Automatica* 43 (2) (2007) 212–225.
- [45] T. Itoh, K. Abe, Hamiltonian-conserving discrete canonical equations based on variational difference quotients, *J. Comput. Phys.* 76 (1) (1988) 85–102.
- [46] G. Quispel, G.S. Turner, Discrete gradient methods for solving ODEs numerically while preserving a first integral, *J. Phys. A: Math. General.* 29 (13) (1996) L341.
- [47] R.I. McLachlan, G. Quispel, N. Robidoux, Geometric integration using discrete gradients, *Philos. Trans. R. Soc. Lond. A: Math., Phys. Eng. Sci.* 357 (1754) (1999) 1021–1045.
- [48] C.J. Budd, M.D. Piggott, Geometric integration and its applications, *Handb. Numer. Anal.* 11 (2003) 35–139.
- [49] J.D. Lambert, *Computational Methods in Ordinary Differential Equations*, Wiley, London, 1973.
- [50] A. Thorin, X. Boutillon, X. Merlhot, J. Lozada, A non-smooth simulation of the dynamics of the grand piano action, in: *Waves 2013*, 2013.